ACS APPLIED MATERIALS & INTERFACES

www.acsami.org Research Article

Electric Field Tuning of Interlayer Coupling in Noncentrosymmetric 3R-MoS_2 with an Electric Double Layer Interface

Xi Zhang,[#] Tongshuai Zhu,[#] Junwei Huang,[#] Qian Wang, Xin Cong, Xiangyu Bi, Ming Tang, Caorong Zhang, Ling Zhou, Dongqin Zhang, Tong Su, Xueting Dai, Kui Meng, Zeya Li, Caiyu Qiu, Wei-Wei Zhao, Ping-Heng Tan, Haijun Zhang, and Hongtao Yuan*

Cite This: *ACS Appl. Mater. Interfaces* 2020, 12, 46900−46907 Read Online

ACCESS | Metrics & More | Article Recommendations | Supporting Information

ABSTRACT: Interlayer coupling in two-dimensional (2D) layered materials plays an important role in controlling their properties. 2H- and 3R-MoS_2 with different stacking orders and the resulting interlayer coupling have been recently discovered to have different band structures and a contrast behavior in valley physics. However, the role of carrier doping in interlayer coupling in 2D materials remains elusive. Here, based on the electric double layer interface, we demonstrated the experimental observation of carrier doping-enhanced interlayer coupling in 3R-MoS_2. A remarkable tuning of interlayer Raman modes can be observed by changing the stacking sequence and carrier doping near their monolayer limit. The modulated interlayer vibration modes originated from the interlayer coupling show a doping-induced blue shift and are supposed to be associated with the interlayer coupling enhancement, which is further verified using our first-principles calculations. Such an electrical control of interlayer coupling of layered materials in an electrical gating geometry provides a new degree of freedom to modify the physical properties in 2D materials.

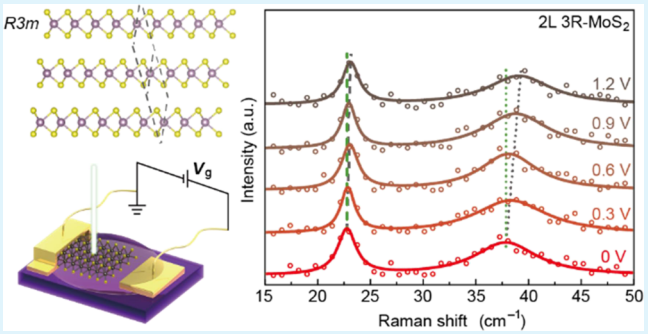

KEYWORDS: *3R-MoS_2, van der Waals, interlayer coupling, electric double layer interface, low-frequency Raman*

INTRODUCTION

The stacking order in two-dimensional (2D) transition metal dichalcogenides (TMDCs) brings different structural symmetries and interlayer couplings, which provide a powerful way to tune their electronic and optical properties.[1−10] Taking MoS_2 as an example, even though the monolayers of 2H- and 3R-MoS_2 are identical, stacking order plays a key role in determining the electronic band structures and physical properties on their bilayer and thicker flakes. For instance, the out-of-plane spin polarization in the valence band at the K and K′ points can only be observed in the 3R-MoS_2 crystal due to the noncentrosymmetric stacking pattern of layers, which in contrast is absent in the 2H-MoS_2 crystal.[7] The recent precise tuning of the twisted angle in bilayer-stacked MoS_2 has shown the powerful capability of tuning the interlayer coupling and realizing emergent electron correlation phenomena.[2,8,11] Carrier doping generally has a direct effect on tuning the position of the Fermi level and subsequent electronic behavior, but its role on the interlayer coupling of MoS_2 has not yet been revealed.

In this work, we employed Raman spectroscopy to probe the interlayer coupling and demonstrated the electric-field controlling effect on MoS_2 with 3R and 2H stacking sequences. By utilizing the electric double layer (EDL) gating technique, we observed clear red/blue shifts in the intralayer/interlayer Raman modes on increasing the doping levels within the ionic liquid gated MoS_2 devices. The blue shift of the interlayer Raman modes directly indicates the enhanced interlayer coupling in the doped system. Based on the first-principles calculations, on increasing the carrier doping, the electron cloud of the doping charge carriers starts to gradually extend into the van der Waals gap. Finally, it forms a three-dimension-like distribution of the doped charges with higher doping levels inside the crystal, implying closer packing between neighboring layers and further enhancement of the interlayer coupling. Our results provide a comprehensive understanding of the doping effect on the interlayer coupling of TMDCs and further guidance for related device design.

Received: July 5, 2020
Accepted: September 15, 2020
Published: September 15, 2020

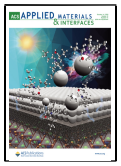

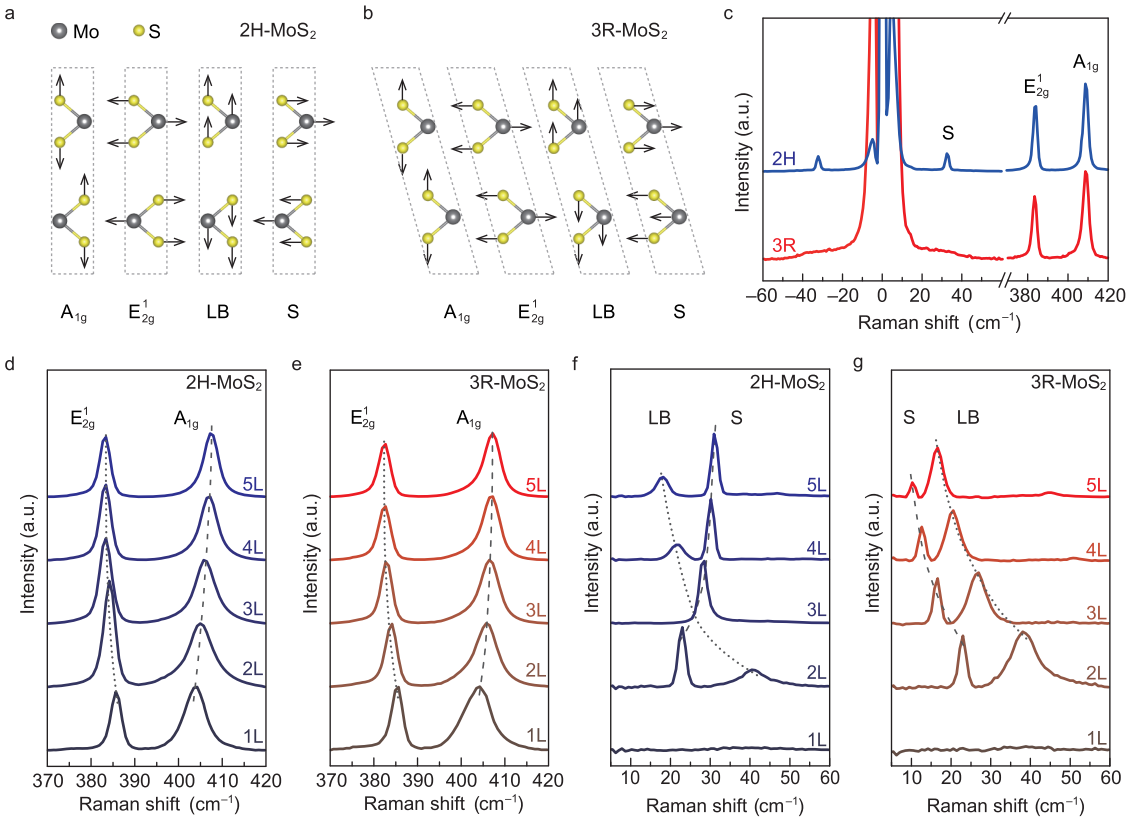

Figure 1. Raman spectra of 2H- and 3R-MoS_2. (a, b) Ball-and-stick crystal structures of 2H- and 3R-MoS_2 (side view). The arrows indicate the atomic displacement of the Raman modes. The polytypes of the MoS_2 sample (2H and 3R) and the symbols of the vibration modes (E^1_{2g}, A_{1g}, S, and LB) are labeled. (c) Raman spectra of bulk 2H- and 3R-MoS_2 using a 532 nm laser line. The polytypes of the sample (2H and 3R) and the symbols of the vibration modes (E^1_{2g}, A_{1g}, and S) are labeled. (d, e) High-frequency Raman spectra of *n*-layer 2H- and 3R-MoS_2 using a 532 nm laser line. The gray dotted and dashed lines indicate the frequency evolution trends of the E^1_{2g} and A_{1g} modes, respectively. The number of layers (1−5 L) is labeled. (f, g) Low-frequency Raman spectra of *n*-layer 2H- and 3R-MoS_2 using a 532 nm laser line. The gray dotted and dashed lines indicate the frequency evolution trends of the LB and S modes, respectively. The number of layers (1−5 L) is labeled.

RESULTS AND DISCUSSION

As a powerful nondamaged method to investigate lattice vibrations, Raman spectroscopy is widely used to investigate the intralayer and interlayer vibration modes and the layer coupling in 2D materials.[12−15] The interlayer vibration modes, including the in-plane shear (S) mode and the out-of-plane layer breathing (LB) mode, have been known to be strongly dependent on the thickness and stacking sequence of materials, which provide abundant information about the interlayer coupling.[16−18] Figure 1a and b shows the schematic diagram for the layer stacking sequence of 2H- and 3R-MoS_2 and their layer displacements of the Raman vibration modes. One can see that the interlayer S and LB modes correspond to layer−layer vibrations when each layer moves as a whole unit. In contrast, the atoms in each layer show different motion directions in the intralayer E^1_{2g} and A_{1g} vibration modes. Therefore, the interlayer and intralayer modes of MoS_2 can serve as fingerprint features for understanding the layer coupling details by Raman spectroscopy. As shown in the Raman spectra of bulk 2H- and 3R-MoS_2 in Figure 1c, the E^1_{2g} and A_{1g} vibration modes at around 384.1 and 408.7 cm^{-1} can be observed in the spectra of both 2H- and 3R-MoS_2 flakes. The S mode appears only in the 2H polytype at 32 cm^{-1}, while it is too weak in the 3R structure and the signal is merged into the background of the Rayleigh line.

Figure 1d and e shows the thickness-dependent Raman spectra of the intralayer modes (E^1_{2g} and A_{1g}) in 2H- and 3R-MoS_2, respectively. These two modes show a contrast thickness-dependent behavior in both 2H- and 3R-MoS_2: with increasing thickness, the A_{1g} mode becomes stiffened, while the E^1_{2g} mode becomes softened. The way to understand this phenomenon is that the interlayer van der Waals force suppresses the atom vibration in the MoS_2 lattice and further leads to a higher intralayer force constant as the layer number increases. As a direct result, both the E^1_{2g} and A_{1g} modes are theoretically supposed to be stiffening (blue shift in the spectra). In our case, the observed blue shift of the A_{1g} peak with the increasing layer number becomes stiffened as expected, whereas the E^1_{2g} peak shows a red shift. This unexpected softening of the E^1_{2g} mode can be explained by the decrease of the long-range Coulombic interaction between the effective charges with the increasing layer number, which is related to the enhancement of the dielectric screening. As a result, the restoring force between the Mo and S atoms is less than that in the monolayer case, which further makes the E^1_{2g} mode to become more softened.[19,20]

The low-frequency interlayer S and LB modes of 2H- and 3R-MoS_2 are shown in Figure 1f and g, respectively. One can see that both the interlayer S and LB modes exhibit an obvious dependence on the detailed stacking information, including the stacking order and the number of stacking layers. For the LB mode, the Raman frequency of both polytypes shows a similar red shift as the number of stacking layers increases. In contrast, the S mode of 2H- and 3R-MoS_2 evolves oppositely,

https://dx.doi.org/10.1021/acsami.0c12165
ACS Appl. Mater. Interfaces 2020, 12, 46900−46907

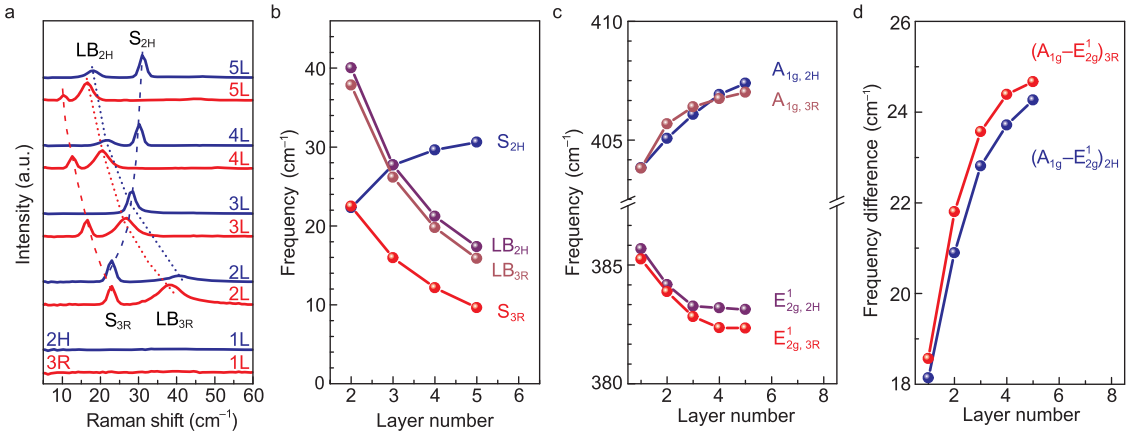

Figure 2. Frequency evolutions in few-layer 2H- and 3R-MoS_2. (a) Comparison of the low-frequency Raman spectra from monolayer to five-layer MoS_2 using a 532 nm laser line. The blue dashed line, blue dotted line, red dashed line, and red dotted line indicate the frequency evolution trends of the S mode of 2H-MoS_2, the LB mode of 2H-MoS_2, the S mode of 3R-MoS_2, and the LB mode of 3R-MoS_2, respectively. The polytypes of the sample and the sample thickness are labeled. (b) Frequency evolutions of the LB and S modes. The polytypes and the vibration modes (S_{2H}, S_{3R}, LB_{2H}, and LB_{3R}) are labeled, and the colors of the labels are the same as the corresponding curves. (c) Frequency evolutions of the E^1_{2g} and A_{1g} modes. The polytypes and the vibration modes ($E^1_{2g,2H}$, $A_{1g,2H}$, $E^1_{2g,3R}$, and $A_{1g,3R}$) are labeled, and the colors of the labels are the same as the corresponding curves. (d) Frequency difference ($\Delta\omega_1$) between the E^1_{2g} and A_{1g} modes [given as $\Delta\omega_1 = \omega(A_{1g}) - \omega(E^1_{2g})$]. The polytypes of the frequency difference [$(A_{1g} - E^1_{2g})_{2H}$ and $(A_{1g} - E^1_{2g})_{3R}$] are labeled, and the colors of the labels are the same as the corresponding curves.

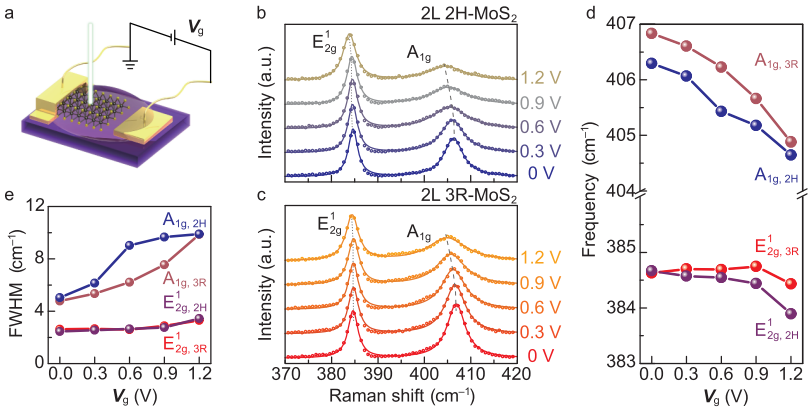

Figure 3. Electric field tuning of the high-frequency Raman spectra in bilayer 2H- and 3R-MoS_2. (a) Schematic diagram of the EDL device. (b, c) High-frequency Raman spectra of bilayer 2H- and 3R-MoS_2 at different gate voltages using a 532 nm laser line. The gray dotted and dashed lines indicate the frequency evolution trends of the E^1_{2g} and A_{1g} modes, respectively. The values of the gate voltages are labeled. (d) Frequency of the E^1_{2g} and A_{1g} modes at different gate voltages. The vibration modes ($E^1_{2g,2H}$, $A_{1g,2H}$, $E^1_{2g,3R}$, and $A_{1g,3R}$) are labeled, and the colors of the labels are the same as the corresponding curves. (e) FWHM of the E^1_{2g} and A_{1g} modes at different gate voltages. The vibration modes ($E^1_{2g,2H}$, $A_{1g,2H}$, $E^1_{2g,3R}$, and $A_{1g,3R}$) are labeled, and the colors of the labels are the same as the corresponding curves.

accompanied by a blue shift in 2H-MoS_2 and a red shift in 3R-MoS_2 on increasing the number of stacking layers. Actually, there are $(n - 1)$ doubly degenerate S and LB modes for the n-layer isotropic MoS_2. Since the peak intensity of most doubly degenerate S and LB modes is very weak, we mainly focus on the strongest S and LB modes marked in Figure 1f and g.

Figure 2a shows the comparison of the low-frequency Raman spectra between 2H- and 3R-MoS_2 with the same number of stacking layers from monolayer to five layers. Obviously, there is no S or LB mode in monolayer MoS_2 since there is no interlayer vibration. When the MoS_2 monolayers are vertically stacked to form bilayer 2H- and 3R-MoS_2 flakes, the S and LB Raman modes are observed at almost the same frequency. In the trilayer case, the S and LB modes overlap into one peak in 2H-MoS_2, while there are still two independent peaks in 3R-MoS_2. As the number of stacking layers increases, the S and LB modes of both 2H- and 3R-MoS_2 exhibit two independent peaks. Note that the frequency of the LB mode is very close between 2H- and 3R-MoS_2, but that of the S mode is very different for all number of stacking layers. The reason for this phenomenon is that the S modes in 2H- and 3R-MoS_2 belong to different vibration modes (S_1 and S_{n-1}), while the LB modes therein come from the same vibration mode (LB_{n-1}), as shown in Figure S3.[21] The difference in the Raman-active modes between 2H and 3R-MoS_2 is caused by the different symmetries directly associated with the stacking sequence, which is further discussed in part 3 of the Supporting Information.

The detailed peak positions of interlayer and intralayer modes as a function of the number of stacking layers are shown in Figure 2b and c. We find that the frequency of the LB mode in 2H-MoS_2 is higher than that in 3R-MoS_2, implying the stronger interlayer coupling in 2H-MoS_2, consistent with a previous report.[16] Meanwhile, the frequency difference ($\Delta\omega_1$) between the E^1_{2g} and A_{1g} modes [defined as $\Delta\omega_1 = \omega(A_{1g}) - \omega(E^1_{2g})$] of 2H-$MoS_2$ is slightly smaller than that of 3R-MoS_2

https://dx.doi.org/10.1021/acsami.0c12165
ACS Appl. Mater. Interfaces 2020, 12, 46900−46907

with the same number of layers, as shown in Figure 2d. As the high-frequency intralayer E^1_{2g} and A_{1g} modes involve vibrations stemming from the interlayer van der Waals force and the intralayer chemical bonds, the two following factors can affect the value of $\Delta\omega_1$ in 2H- and 3R-MoS_2. First, the frequency of the intralayer phonon mode of MoS_2 with a certain thickness is mainly determined by the intralayer chemical bonds, which will be affected by doping, and hence, the $\Delta\omega_1$ value will be influenced. Second, the variation in the stacking sequence can generate a certain difference in the interlayer coupling, which further influences the value of $\Delta\omega_1$. As expected, the values of $\Delta\omega_1$ for 2H- and 3R-MoS_2 with the same thickness are related to the interlayer coupling under relatively ideal conditions with less doping: the larger the value of $\Delta\omega_1$, the stronger the interlayer coupling. Interestingly, $\Delta\omega_1$ in 2H-MoS_2 has consistently smaller values than that of 3R-MoS_2, even though the interlayer coupling of 2H-MoS_2 is slightly stronger than that of 3R-MoS_2, as exhibited in the result of the low-frequency Raman mode. As discussed above, this phenomenon can be explained with the experimental samples of 2H- and 3R-MoS_2 under different doping levels induced by the growing processes of the samples, and the slight doping will have a certain effect on the chemical bonds, indicating that the value of $\Delta\omega_1$ is more obviously affected by chemical bonds. The result is consistent with the fact that the frequency of the intralayer mode is mainly dominated by the strength of the intralayer chemical bonds since the chemical bonds are much stronger than the van der Waals force. In addition, the slight difference in frequency between monolayer 2H- and 3R-MoS_2 might come from the influence of the substrate or the doping level variation of the tested flakes.

In order to understand the electron doping effect on the vibration modes, we applied the EDL gating technique in 2H- and 3R-MoS_2 to engineer the interlayer coupling, as shown in the schematic diagram in Figure 3a. The EDL interface with ionic liquids as a gate dielectric has been well known as a powerful tool to modulate the electronic states in semiconductors.[22,23] At the functionalized liquid/solid EDL interface, serving as a nanogap capacitor with huge capacitance, charge carriers over a wide density range can be accumulated.[24−26] Figure 3b and c shows the high-frequency Raman spectra of bilayer 2H- and 3R-MoS_2 under electrical control within an EDL interface. The frequency and the corresponding full width at half maximum (FWHM) of Raman spectra as a function of gate voltages (V_g) are plotted in Figure 3d and e. Two remarkable features need to be addressed here. First, as the V_g increases, the softening of the A_{1g} mode can gradually reach a level as high as 1.6 cm^{-1} for 2H-MoS_2 and 2 cm^{-1} for 3R-MoS_2, exhibiting the clear dependence on carrier doping. In comparison, the frequency shift of the E^1_{2g} mode is smaller in both 2H- and 3R-MoS_2. Second, the FWHM of the A_{1g} mode increases significantly by 5 cm^{-1} for the achieved maximum doping level in both 2H- and 3R-MoS_2, whereas the FWHM of the E^1_{2g} mode shows a minor change of only 0.7 cm^{-1}. These features are supposed to be associated with the electron−phonon coupling between the band-edge valley electrons and the A_{1g} phonons when the occupation of the valley state is perturbed by carrier doping.[27] In contrast, the electron−phonon coupling is weak between the band-edge valley electrons and the E^1_{2g} phonons.[27] Since electron doping and Fermi level tuning occur near the conduction band edge for 2H- and 3R-MoS_2, the evolution of Raman vibration frequency in 3R-MoS_2 tuned by EDL geometry shows a similar trend to that in 2H-MoS_2, and the corresponding evolutions are consistent with the previous reports based on the electrochemical and chemical doping in 2H-MoS_2.[27,28] However, these similarities are all about the E^1_{2g} and A_{1g} vibration modes, and both of them are intralayer vibration modes. These similarities are normal and inevitable since the two structures share exactly the same monolayer structure. In addition to the electric field tuning results in bilayer MoS_2, we also applied the EDL gating technique in 2H- and 3R-MoS_2 with different thicknesses, as shown in Figures S4 and S5. We find that, with increasing thickness, the gating tunability on the E^1_{2g} and A_{1g} modes gets weaker since the EDL gating effect is only a surface effect associated with electron accumulation with surface band bending. More details are given in part 4 of the Supporting Information.

To investigate the influence of the electron doping on the interlayer coupling, the V_g-dependent Raman spectra of bilayer 3R-MoS_2 in the low-frequency region are shown in Figure 4a.

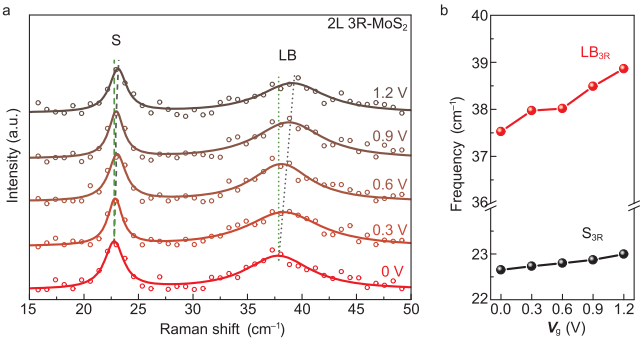

Figure 4. Electric field tuning of the low-frequency Raman modes in bilayer 3R-MoS_2. (a) Low-frequency Raman spectra of bilayer 3R-MoS_2 at different gate voltages using a 532 nm laser line. The gray dotted and dashed lines indicate the frequency evolution trends of the LB and S modes, respectively. The green dotted and dashed lines indicate the vertical direction. The values of the gate voltages are labeled. (b) Frequency of the S and LB modes at different gate voltages. The vibration modes (S_{3R} and LB_{3R}) are labeled, and the colors of the labels are the same as the corresponding curves.

We use the following method to confirm the frequency of the S and LB modes in 3R-MoS_2 [$\omega(S_{3R})$ and $\omega(LB_{3R})$], ensuring that the frequency is more accurate. Both the Stokes (S_S and LB_S) and Anti-Stokes (S_{AS} and LB_{AS}) S and LB modes are fitted using the Lorentz fitting. Then, we take $\omega(S_{3R}) = \frac{\omega(S_S) + |\omega(S_{AS})|}{2}$ and $\omega(LB_{3R}) = \frac{\omega(LB_S) + |\omega(LB_{AS})|}{2}$ as the frequencies of the S and LB modes in 3R-MoS_2. As the electron doping level increases (V_g from 0 to 1.2 V), a monotonic increase of the frequency of both S and LB modes is clearly observed, which is more pronounced for the LB mode. Such a kind of electrical control on the low-frequency Raman spectra has never been reported before.

Three important characteristic features shown in Figure 4 can be addressed here. First, both S and LB modes show blue shifts with increasing V_g, showing the typical behavior of the enhanced interlayer coupling. Second, the frequency of the S mode stiffens by 0.3 cm^{-1} with the increasing doping level, while the blue shift can occur more easily for the LB mode by 1.3 cm^{-1} (Figure 4b). Third, the low-frequency Raman modes have less shift than the high-frequency ones under electrical control because the intralayer chemical bonds are more sensitive to electronic doping than the interlayer van der

https://dx.doi.org/10.1021/acsami.0c12165
ACS Appl. Mater. Interfaces 2020, 12, 46900−46907

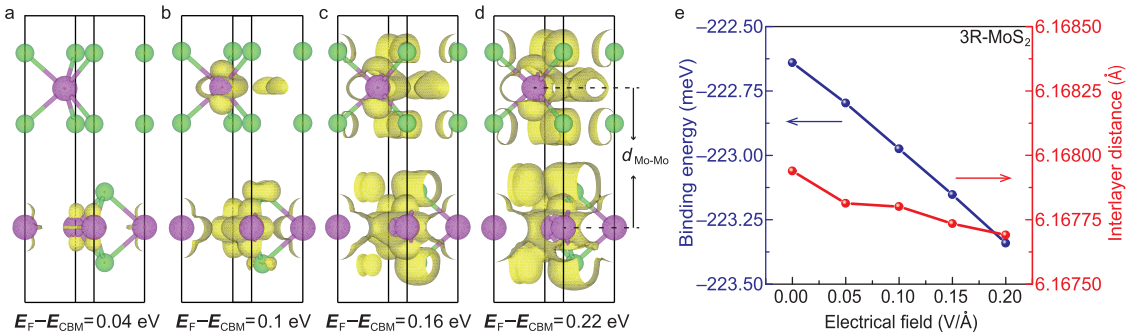

Figure 5. Partial charge density, interlayer binding energy, and interlayer distance of 3R-MoS_2. (a−d) Partial charge density of 3R-MoS_2 in the energy range from E_{CBM} to E_F at 0.04 eV (2.27×10^{13} cm^{-2}), 0.1 eV (1.91×10^{14} cm^{-2}), 0.16 eV (4.34×10^{14} cm^{-2}), and 0.22 eV (6.65×10^{14} cm^{-2}). The yellow area represents the distribution of the charge density with an isosurface value of 0.0004 e/$Bohr^3$ based on calculations. (e) Interlayer binding energy and interlayer distance of 3R-MoS_2 under an electrical field. The blue dots represent the interlayer binding energy, and the red dots represent the interlayer distance.

Waals interactions, which is consistent with the above-mentioned discussion that the intralayer chemical bonds can be affected by doping.

To understand the physical mechanism of the doping-enhanced interlayer coupling, we performed the first-principles calculations for both 2H- and 3R-MoS_2. We plotted the partial charge density in the energy range from E_{CBM} to E_F (E_F and E_{CBM} are the energy levels of the Fermi surface and conduction band minimum) as shown in Figure 5 to understand the distribution of the doped charges in the crystal structure under different doping levels. We chose several doping levels with the value of the energy ranging from E_{CBM} to E_F covering 0.04 eV (the calculated sheet carrier density is 2.27×10^{13} cm^{-2}) to 0.22 eV (the calculated sheet carrier density is 6.65×10^{14} cm^{-2}) to simulate the accumulated carrier doping achieved at the EDL interface in the liquid gating experiments. One can clearly see that, on increasing the doping level, the electron cloud of the doped carriers in each layer starts to have an extended distribution into the van der Waals gap and even tends to overlap with the electron cloud from its neighboring layers, implying a stronger interaction and closer stacking between the two adjacent layers.

Since such an enhanced interlayer interaction can also be associated with the doping-induced evolution of the interlayer lattice parameter of 3R-MoS_2, we further calculated the interlayer binding energy $E_{binding}$ under different doping levels, which corresponds to a certain magnitude of the applied electric field across the 3R-MoS_2 slab. We defined $E_{binding} = E_{bi} - 2E_{mon}$ as the interlayer binding energy, which is the amount of energy required to separate a monolayer from the system of bilayer 3R-MoS_2. E_{bi} and E_{mon} are the total energy of bilayer and monolayer 3R-MoS_2, respectively. As shown in Figure 5e, as the doping level increases (also the applied electric field becomes larger), the interlayer lattice parameter d_{Mo-Mo} (the distance between the Mo atom layers in two adjacent MoS_2 layers) of 3R-MoS_2 decreases and the absolute value of the interlayer binding energy increases, implying closer layer stacking and doping-enhanced interlayer coupling in 3R-MoS_2. A similar evolution trend for both the interlayer lattice parameter and the interlayer binding energy with increasing doping level has also been observed in the 2H-MoS_2 case, as shown in Figure S9, indicating that the phenomenon of interlayer coupling enhancement may also exist in 2H-MoS_2. Compared with 3R-MoS_2 quantitatively, more noticeable changes are observed in the interlayer binding energy and interlayer distance of 2H-MoS_2, which may be ascribed to the symmetries of 2H- and 3R-MoS_2. A dipole moment will form when an electric field is applied to MoS_2. The interaction between the dipoles with centrosymmetry may be stronger, which leads to the more evident changes in the interlayer binding energy and interlayer distance of centrosymmetrically stacked 2H-MoS_2 than those of the noncentrosymmetrically stacked 3R-MoS_2. The above calculation results, involving the decrease in the interlayer lattice parameter and the increase in the absolute value of interlayer binding energy for both 2H- and 3R-MoS_2, imply that the doping-enhanced interlayer coupling might serve as a universal phenomenon that can be generally observed in 2D layered materials.

■ CONCLUSIONS

In summary, we reported the interlayer coupling evolution in MoS_2 with different stacking sequences and found out that the interlayer coupling in 3R-MoS_2 is smaller than that in 2H-MoS_2. The interlayer coupling can be experimentally tuned through electrostatic doping by reducing the interlayer lattice parameter. Such an approach to combine the EDL gating technique with Raman spectroscopy provides an effective way to understand the interlayer coupling in 2D materials.

■ EXPERIMENTAL SECTION

Device Fabrication. Ultrathin 2H- and 3R-MoS_2 flakes were prepared using the mechanical exfoliation method onto a silicon wafer with a 300 nm thick silicon dioxide layer. The number of stacking layers of 2H- and 3R-MoS_2 flakes was identified by both optical contrast and Raman spectroscopy. Electrical contacts in the EDL devices were fabricated using a standard electron beam lithography (EBL) process. In all devices, Ti (6 nm)/Au (50 nm) patterns were deposited as the electrodes using e-beam evaporation. Lift-off was carried out by immersing the sample into an acetone bath at 50 °C for about 30 min.

Raman Measurements. Raman measurements were performed using a confocal Raman spectrometer (WITec Alpha300). A signal was collected through a long working distance × 50 objective lens, dispersed with a 1800 g/mm grating. An ionic liquid (DEME-TFSI) was drop-cast on top of the devices, covering both flakes and the gold metal pad for gating. Electrical measurements were carried out using a Keithley 2400 source meter. In order to protect the sample, all V_g-dependent Raman measurements were performed in a nitrogen ambient environment.

First-Principles Calculations. The first-principles calculations were performed using the Vienna ab initio simulation package (VASP)[29,30] and the generalized gradient approximation with the

https://dx.doi.org/10.1021/acsami.0c12165
ACS Appl. Mater. Interfaces 2020, 12, 46900−46907

Perdew–Burke–Ernzerhof (PBE)[31,32] type exchange–correlation functional was adopted. The kinetic energy cutoff was fixed to 430 eV, and the correction of van der Waals coupling with the optB86b-vdw functional was employed, which was proved to be accurate in describing the structural properties of layered materials.[33] The lattice constants of 2H-MoS_2 (a = 3.169 Å) and 3R-MoS_2 (a = 3.167 Å) were obtained through full relaxation with a total energy tolerance of 10^{-6} eV and a Γ-centered k-grid of 10 × 10 × 6. For MoS_2 layers, the lattice constants were fixed with the bulk ones, and a 20 Å vacuum layer was used to eliminate the interaction between each layer and the atoms were fully relaxed with a total energy tolerance of 10^{-6} eV and a Γ-centered k-grid of 10 × 10 × 1. We calculated the phonon frequencies for one layer to four layers of 2H- and 3R-MoS_2 at the Brillouin zone center using the density functional perturbation theory (DFPT)[34] as implemented in the PHONOPY[35] code with a 2 × 2 × 1 supercell.

To simulate the accumulated carrier doping achieved in the liquid gating experiments, we calculated the partial charge density at different energy ranges from E_{CBM} to E_F. We can see the distribution of increased charge density as the doping level increases (also the Fermi level increases). Thus, we assume that the partial charge density in the energy range from E_{CBM} to E_F is the charge density of the doped electrons. We also calculated the atom position of bilayer 2H- and 3R-MoS_2 at different values of the electric field along the z axis with the EFIELD tag using which we obtained the distance between the two layers. We determined the carrier density by calculating the partial charge density in the energy range from E_{CBM} to E_F and integrated the whole volume to get the charge of a unit cell at different energy ranges from E_{CBM} to E_F. We also obtained the binding energy between bilayers and each monolayer of 2H- and 3R-MoS_2. We defined $E_{binding} = E_{bi} - 2E_{mon}$, where $E_{binding}$ is the interlayer binding energy that represents the amount of energy required to separate the monolayer from the system of bilayer 3R-MoS_2, and E_{bi} and E_{mon} are the total energy of bilayer and monolayer 3R-MoS_2.

■ ASSOCIATED CONTENT

Supporting Information

The Supporting Information is available free of charge at https://pubs.acs.org/doi/10.1021/acsami.0c12165.

Resonance Raman spectra; comparison of the high-frequency Raman spectra; comparison of the low-frequency Raman modes; gate-dependent evolution of frequency difference; details of the peak position analysis; theoretical calculations of the deformation charge density; theoretical calculation details of the interlayer binding energy, interlayer distance, and phonon dispersion; partial charge density of 3R-MoS_2 from E_F to E_{VBM}; and comparison of experimental and calculated results of the Raman vibration modes (PDF)

■ AUTHOR INFORMATION

Corresponding Author

Hongtao Yuan − *National Laboratory of Solid State Microstructures, College of Engineering and Applied Sciences, and Collaborative Innovation Center of Advanced Microstructures, Nanjing University, Nanjing 210093, P. R. China*; Email: htyuan@nju.edu.cn

Authors

Xi Zhang − *National Laboratory of Solid State Microstructures, School of Physics, College of Engineering and Applied Sciences, and Collaborative Innovation Center of Advanced Microstructures, Nanjing University, Nanjing 210093, P. R. China*

Tongshuai Zhu − *National Laboratory of Solid State Microstructures, School of Physics, and Collaborative Innovation Center of Advanced Microstructures, Nanjing University, Nanjing 210093, P. R. China*

Junwei Huang − *National Laboratory of Solid State Microstructures, College of Engineering and Applied Sciences, and Collaborative Innovation Center of Advanced Microstructures, Nanjing University, Nanjing 210093, P. R. China*

Qian Wang − *School of Chemistry and Chemical Engineering, Nanjing University, Nanjing 210023, P. R. China*

Xin Cong − *State Key Laboratory of Superlattices and Microstructures, Institute of Semiconductors, Chinese Academy of Sciences, Beijing 100083, P. R. China*

Xiangyu Bi − *National Laboratory of Solid State Microstructures, College of Engineering and Applied Sciences, and Collaborative Innovation Center of Advanced Microstructures, Nanjing University, Nanjing 210093, P. R. China*

Ming Tang − *National Laboratory of Solid State Microstructures, School of Physics, College of Engineering and Applied Sciences, and Collaborative Innovation Center of Advanced Microstructures, Nanjing University, Nanjing 210093, P. R. China*

Caorong Zhang − *National Laboratory of Solid State Microstructures, School of Physics, College of Engineering and Applied Sciences, and Collaborative Innovation Center of Advanced Microstructures, Nanjing University, Nanjing 210093, P. R. China*

Ling Zhou − *National Laboratory of Solid State Microstructures, College of Engineering and Applied Sciences, and Collaborative Innovation Center of Advanced Microstructures, Nanjing University, Nanjing 210093, P. R. China*

Dongqin Zhang − *National Laboratory of Solid State Microstructures, School of Physics, and Collaborative Innovation Center of Advanced Microstructures, Nanjing University, Nanjing 210093, P. R. China; Department of Physics, China Jiliang University, Hangzhou 310018, P. R. China*

Tong Su − *National Laboratory of Solid State Microstructures, College of Engineering and Applied Sciences, and Collaborative Innovation Center of Advanced Microstructures, Nanjing University, Nanjing 210093, P. R. China*

Xueting Dai − *National Laboratory of Solid State Microstructures, College of Engineering and Applied Sciences, and Collaborative Innovation Center of Advanced Microstructures, Nanjing University, Nanjing 210093, P. R. China*

Kui Meng − *National Laboratory of Solid State Microstructures, College of Engineering and Applied Sciences, and Collaborative Innovation Center of Advanced Microstructures, Nanjing University, Nanjing 210093, P. R. China*

Zeya Li − *National Laboratory of Solid State Microstructures, College of Engineering and Applied Sciences, and Collaborative Innovation Center of Advanced Microstructures, Nanjing University, Nanjing 210093, P. R. China*

Caiyu Qiu − *National Laboratory of Solid State Microstructures, College of Engineering and Applied Sciences, and Collaborative Innovation Center of Advanced Microstructures, Nanjing University, Nanjing 210093, P. R. China*

Wei-Wei Zhao − *School of Chemistry and Chemical Engineering, Nanjing University, Nanjing 210023, P. R. China*; orcid.org/0000-0002-8179-4775

Ping-Heng Tan − *State Key Laboratory of Superlattices and Microstructures, Institute of Semiconductors, Chinese Academy of Sciences, Beijing 100083, P. R. China*

https://dx.doi.org/10.1021/acsami.0c12165
ACS Appl. Mater. Interfaces 2020, 12, 46900−46907

Haijun Zhang − *National Laboratory of Solid State Microstructures, School of Physics, and Collaborative Innovation Center of Advanced Microstructures, Nanjing University, Nanjing 210093, P. R. China*

Complete contact information is available at: https://pubs.acs.org/10.1021/acsami.0c12165

Author Contributions

[#]X.Z., T.S.Z. and J.W.H. contributed equally to this work. H.T.Y., H.J.Z., and P.H.T. conceived the project and designed the experiments. X.Z., M.T., C.R.Z., and L.Z. performed device fabrication. X.Z., Q.W., W.W.Z., T.S., X.T.D., and K.M. carried out the optical measurements. X.Z., T.S.Z., J.W.H., X.Y.B., Z.Y.L., X.C., and C.Y.Q. analyzed the data. T.S.Z. and D.Q.Z. carried out the theoretical calculations. X.Z. and H.T.Y. wrote the paper with all authors' input.

Notes

The authors declare no competing financial interest.

■ ACKNOWLEDGMENTS

This research was supported by the National Natural Science Foundation of China (91750101, 21733001, 51861145201, and 11674165), the National Key Basic Research Program of the Ministry of Science and Technology of China (2018YFA0306200), the Fundamental Research Funds for the Central Universities (021314380078, 021314380104, 021314380147, and 020414380149), the Priority Academic Program Development of Jiangsu Higher Education Institutions (021314416201), the Fok Ying-Tong Education Foundation of China (Grant No. 161006), and the Jiangsu Key Laboratory of Artificial Functional Materials.

■ REFERENCES

(1) Yan, J.; Xia, J.; Wang, X.; Liu, L.; Kuo, J. L.; Tay, B. K.; Chen, S.; Zhou, W.; Liu, Z.; Shen, Z. X. Stacking-Dependent Interlayer Coupling in Trilayer MoS_2 with Broken Inversion Symmetry. *Nano Lett.* **2015**, *15*, 8155−8161.

(2) Yeh, P.-C.; Jin, W.; Zaki, N.; Kunstmann, J.; Chenet, D.; Arefe, G.; Sadowski, J. T.; Dadap, J. I.; Sutter, P.; Hone, J.; Osgood, R. M., Jr. Direct Measurement of the Tunable Electronic Structure of Bilayer MoS_2 by Interlayer Twist. *Nano Lett.* **2016**, *16*, 953−959.

(3) Liu, K.; Zhang, L.; Cao, T.; Jin, C.; Qiu, D.; Zhou, Q.; Zettl, A.; Yang, P.; Louie, S. G.; Wang, F. Evolution of Interlayer Coupling in Twisted Molybdenum Disulfide Bilayers. *Nat. Commun.* **2014**, *5*, 4966.

(4) Yuan, H.; Bahramy, M. S.; Morimoto, K.; Wu, S.; Nomura, K.; Yang, B. J.; Shimotani, H.; Suzuki, R.; Toh, M.; Kloc, C.; Xu, X.; Arita, R.; Nagaosa, N.; Iwasa, Y. Zeeman-Type Spin Splitting Controlled by an Electric Field. *Nat. Phys.* **2013**, *9*, 563−569.

(5) Jiang, T.; Liu, H.; Huang, D.; Zhang, S.; Li, Y.; Gong, X.; Shen, Y. R.; Liu, W. T.; Wu, S. Valley and Band Structure Engineering of Folded MoS_2 Bilayers. *Nat. Nanotechnol.* **2014**, *9*, 825−829.

(6) Hsu, W. T.; Zhao, Z. A.; Li, L. J.; Chen, C. H.; Chiu, M. H.; Chang, P. S.; Chou, Y. C.; Chang, W. H. Second Harmonic Generation from Artificially Stacked Transition Metal Dichalcogenide Twisted Bilayers. *ACS Nano* **2014**, *8*, 2951−2958.

(7) Suzuki, R.; Sakano, M.; Zhang, Y. J.; Akashi, R.; Morikawa, D.; Harasawa, A.; Yaji, K.; Kuroda, K.; Miyamoto, K.; Okuda, T.; Ishizaka, K.; Arita, R.; Iwasa, Y. Valley-Dependent Spin Polarization in Bulk MoS_2 with Broken Inversion Symmetry. *Nat. Nanotechnol.* **2014**, *9*, 611−617.

(8) Huang, S.; Ling, X.; Liang, L.; Kong, J.; Terrones, H.; Meunier, V.; Dresselhaus, M. S. Probing the Interlayer Coupling of Twisted Bilayer MoS_2 Using Photoluminescence Spectroscopy. *Nano Lett.* **2014**, *14*, 5500−5508.

(9) Akashi, R.; Ochi, M.; Bordács, S.; Suzuki, R.; Tokura, Y.; Iwasa, Y.; Arita, R. Two-Dimensional Valley Electrons and Excitons in Noncentrosymmetric 3R-MoS_2. *Phys. Rev. Appl.* **2015**, *4*, No. 014002.

(10) Zhao, M.; Ye, Z.; Suzuki, R.; Ye, Y.; Zhu, H.; Xiao, J.; Wang, Y.; Iwasa, Y.; Zhang, X. Atomically Phase-Matched Second-Harmonic Generation in a 2D crystal. *Light: Sci. Appl.* **2016**, *5*, No. e16131.

(11) Van der Zande, A. M.; Kunstmann, J.; Chernikov, A.; Chenet, D. A.; You, Y.; Zhang, X.; Huang, P. Y.; Berkelbach, T. C.; Wang, L.; Zhang, F.; Hybertsen, M. S.; Muller, D. A.; Reichman, D. R.; Heinz, T. F.; Hone, J. C. Tailoring the Electronic Structure in Bilayer Molybdenum Disulfide via Interlayer Twist. *Nano Lett.* **2014**, *14*, 3869−3875.

(12) Li, H.; Zhang, Q.; Yap, C. C. R.; Tay, B. K.; Edwin, T. H. T.; Olivier, A.; Baillargeat, D. From Bulk to Monolayer MoS_2: Evolution of Raman Scattering. *Adv. Funct. Mater.* **2012**, *22*, 1385−1390.

(13) Wang, Y.; Xiao, J.; Zhu, H.; Li, Y.; Alsaid, Y.; Fong, K. Y.; Zhou, Y.; Wang, S.; Shi, W.; Wang, Y.; Zettl, A.; Reed, E. J.; Zhang, X. Structural Phase Transition in Monolayer $MoTe_2$ Driven by Electrostatic Doping. *Nature* **2017**, *550*, 487−491.

(14) Tan, P. H.; Han, W. P.; Zhao, W. J.; Wu, Z. H.; Chang, K.; Wang, H.; Wang, Y. F.; Bonini, N.; Marzari, N.; Pugno, N.; Savini, G.; Lombardo, A.; Ferrari, A. C. The Shear Mode of Multilayer Graphene. *Nat. Mater.* **2012**, *11*, 294−300.

(15) Zhang, X.; Tan, Q. H.; Wu, J. B.; Shi, W.; Tan, P. H. Review on the Raman Spectroscopy of Different Types of Layered Materials. *Nanoscale* **2016**, *8*, 6435−6450.

(16) Van Baren, J.; Ye, G.; Yan, J. A.; Ye, Z.; Rezaie, P.; Yu, P.; Liu, Z.; He, R.; Lui, C. H. Stacking-Dependent Interlayer Phonons in 3R and 2H MoS_2. *2D Mater* **2019**, *6*, 025022.

(17) Zhang, X.; Han, W. P.; Wu, J. B.; Milana, S.; Lu, Y.; Li, Q. Q.; Ferrari, A. C.; Tan, P. H. Raman Spectroscopy of Shear and Layer Breathing Modes in Multilayer MoS_2. *Phys. Rev. B: Condens. Matter Mater. Phys.* **2013**, *87*, 115413.

(18) Puretzky, A. A.; Liang, L.; Li, X.; Xiao, K.; Wang, K.; Mahjouri-Samani, M.; Basile, L.; Idrobo, J. C.; Sumpter, B. G.; Meunier, V.; Geohegan, D. B. Low-frequency Raman Fingerprints of Two-Dimensional Metal Dichalcogenide Layer Stacking Configurations. *ACS Nano* **2015**, *9*, 6333−6342.

(19) Lee, C.; Yan, H.; Brus, L. E.; Heinz, T. F.; Hone, J.; Ryu, S. Anomalous Lattice Vibrations of Single- and Few-Layer MoS_2. *ACS Nano* **2010**, *4*, 2695−2700.

(20) Molina-Sánchez, A.; Wirtz, L. Phonons in Single-Layer and Few-Layer MoS_2 and WS_2. *Phys. Rev. B* **2011**, *84*, 155413.

(21) Liang, L.; Puretzky, A. A.; Sumpter, B. G.; Meunier, V. Interlayer Bond Polarizability Model for Stacking Dependent Low-Frequency Raman Scattering in Layered Materials. *Nanoscale* **2017**, *9*, 15340−15355.

(22) Lu, J. M.; Zheliuk, O.; Leermakers, I.; Yuan, N. F. Q.; Zeitler, U.; Law, K. T.; Ye, J. T. Evidence for Two-Dimensional Ising Superconductivity in Gated MoS_2. *Science* **2015**, *350*, 1353−1357.

(23) Yuan, H. T.; Toh, M.; Morimoto, K.; Tan, W.; Wei, F.; Shimotani, H.; Kloc, C.; Iwasa, Y. Liquid-Gated Electric-Double-Layer Transistor on Layered Metal Dichalcogenide, SnS_2. *Appl. Phys. Lett.* **2011**, *98*, No. 012102.

(24) Shimotani, H.; Asanuma, H.; Takeya, J.; Iwasa, Y. Electrolyte-Gated Charge Accumulation in Organic Single Crystals. *Appl. Phys. Lett.* **2006**, *89*, 203501.

(25) Shimotani, H.; Asanuma, H.; Tsukazaki, A.; Ohtomo, A.; Kawasaki, M.; Iwasa, Y. Insulator-to-Metal Transition in ZnO by Electric Double Layer Gating. *Appl. Phys. Lett.* **2007**, *91*, No. 082106.

(26) Cho, J. H.; Lee, J.; He, Y.; Kim, B. S.; Lodge, T. P.; Frisbie, C. D. High-Capacitance Ion Gel Gate Dielectrics with Faster Polarization Response Times for Organic Thin Film Transistors. *Adv. Mater.* **2008**, *20*, 686−690.

(27) Chakraborty, B.; Bera, A.; Muthu, D. V. S.; Bhowmick, S.; Waghmare, U. V.; Sood, A. K. Symmetry-Dependent Phonon Renormalization in Monolayer MoS_2 Transistor. *Phys. Rev. B: Condens. Matter Mater. Phys.* **2012**, *85*, 161403.

(28) Wang, Z.; Zhao, G.; Luo, R.; Johnson, I.; Kashani, H.; Chen, M. Chemical Doping Induced Zone-Edge Phonon Renormalization in Single-Layer MoS_2. *Phys. Rev. B: Condens. Matter Mater. Phys.* **2019**, *100*, No. 085401.
(29) García, A.; Cohen, M. L. First-principles ionicity scales. I. Charge Asymmetry in the Solid State. *Phys. Rev. B: Condens. Matter Mater. Phys.* **1993**, *47*, 4215−4220.
(30) Kresse, G.; Furthmüller, J. Efficient Iterative Schemes for *Ab Initio* Total-Energy Calculations Using a Plane-Wave Basis set. *Phys. Rev. B: Condens. Matter Mater. Phys.* **1996**, *54*, 11169−11186.
(31) Blöchl, P. E. Projector Augmented-Wave Method. *Phys. Rev. B: Condens. Matter Mater. Phys.* **1994**, *50*, 17953−17979.
(32) Perdew, J. P.; Burke, K.; Ernzerhof, M. Generalized Gradient Approximation Made Simple. *Phys. Rev. Lett.* **1996**, *77*, 3865−3868.
(33) Klimeš, J.; Bowler, D. R.; Michaelides, A. Van der Waals Density Functionals Applied to Solids. *Phys. Rev. B: Condens. Matter Mater. Phys.* **2011**, *83*, 195131.
(34) Gonze, X.; Lee, C. Dynamical matrices, Born Effective Charges, Dielectric Permittivity Tensors, and Interatomic Force Constants from Density-Functional Perturbation Theory. *Phys. Rev. B: Condens. Matter Mater. Phys.* **1997**, *55*, 10355−10368.
(35) Togo, A.; Tanaka, I. First Principles Phonon Calculations in Materials Science. *Scripta Mater.* **2015**, *108*, 1−5.

https://dx.doi.org/10.1021/acsami.0c12165
ACS Appl. Mater. Interfaces 2020, 12, 46900−46907